1 Quantifying black carbon light absorption enhancement by a novel

2 statistical approach

3 **Cheng Wu[1,2], Dui Wu[1,2,3], Jian Zhen Yu[4,5,6]**

4

5 [1]Institute of Mass Spectrometer and Atmospheric Environment, Jinan University, Guangzhou 510632, China

6 [2]Guangdong Provincial Engineering Research Center for on-line source apportionment system of air

7 pollution, Guangzhou 510632, China

8 [3]Institute of Tropical and Marine Meteorology, China Meteorological Administration, Guangzhou 510080,

9 China

10 [4]Division of Environment, Hong Kong University of Science and Technology, Clear Water Bay, Hong Kong,

11 China

12 [5]Atmospheric Research Centre, Fok Ying Tung Graduate School, Hong Kong University of Science and

13 Technology, Nansha, China

14 [6]Department of Chemistry, Hong Kong University of Science and Technology, Clear Water Bay, Hong

15 Kong, China

16 *Corresponding to*: Cheng Wu (wucheng.vip@foxmail.com) and Jian Zhen Yu (jian.yu@ust.hk)

17

18 Abstract

19   Black carbon (BC) particles in the atmosphere can absorb more light when coated by non-absorbing

20 or weakly absorbing materials during atmospheric aging, due to the lensing effect. In this study, the light

21 absorption enhancement factor, E_{abs}, was quantified using one year's measurement of mass absorption

22 efficiency (MAE) in the Pearl River Delta region (PRD). A new approach for calculating primary MAE

23 (MAE_p), the key for E_{abs} estimation, is demonstrated using the Minimum R Squared (MRS) method, exploring

24 the inherent source independency between BC and its coating materials. The annual average E_{abs} is found to

25 be 1.52, exhibiting a clear seasonal pattern with higher values in summer and lower in the winter. Elevated

26 E_{abs} in the rainy summer season is likely associated with aged air masses dominating from marine origin,

27 along with long-range transport of biomass burning influenced air masses from Southeast Asia. E_{abs} induced

28 by hygroscopic growth at elevated RH could be as high as 1.3. Core-shell Mie simulations along with

29 measured E_{abs} and Angstrom absorption exponent (AAE) constraints suggest that in the PRD, the coating

30 materials are unlikely to be dominated by brown carbon and the coating thickness is higher in the rainy season

31 than the dry season. A negative correlation is found between $AAE_{470-660}$ and RH, suggesting a dominant

32 particle size of D_{core} = 130 nm and D_{shell}/D_{core} range of 2 to 4.

33

1 Introduction

35   Originating from incomplete combustion, black carbon (BC) is a crucial constituent of atmospheric

36   aerosols, and is an air pollutant itself, having an adverse health impacts on humans (Suglia et al., 2008). BC

37   has also been recognized as the third most important climate forcer due to its broad light absorbing capability

38   across the UV-Vis-IR spectrum (IPCC, 2013). BC can alter the climate in a variety of ways, including by

39   direct forcing (Bond et al., 2011), affecting cloud cover (Koch and Del Genio, 2010) and precipitation (Tao

40   et al., 2012), reducing the albedo of snow and ice (Hansen and Nazarenko, 2004) and causing surface dimming

41   (Wild, 2011). The climate effects of BC can be global or regional (Ramanathan and Carmichael, 2008). A

42   recent study found BC can modify planetary boundary layer meteorology, and thus enhance local pollution

43   indirectly (Ding et al., 2016). However, due to its variable optical characteristics induced during atmospheric

44   aging, large uncertainties still exist in estimating the radiative forcing from BC. Optical properties of BC can

45   be predicted by knowing the mass concentration, mixing state and size distribution, which collectively serve

46   as the cornerstone for modeling the climate effect of BC. In 3D modeling studies, to conserve computational

47   resources, the mass absorption efficiency (MAE) or mass absorption cross-section (MAC) is widely used to

48   convert black carbon mass concentration to light absorption coefficient (σ_{abs}). MAE is a quantity to describe

49   the light absorption ability per unit EC mass:

50
$$\text{MAE} \ (m^2 \ g^{-1}) = \frac{absorption \ coefficient \ \sigma_{abs} \ (Mm^{-1})}{EC \ mass \ concentration \ (\mu g \ m^{-3})} \tag{1}$$

51   As a fundamental input parameter, MAE has a critical impact on BC's radiative forcing estimation in

52   climate modeling studies. Mixing state is one of the governing factors affecting MAE. Light absorption of

53   soot particles is enhanced when coated with non-absorbing materials (Fuller et al., 1999) or weakly absorbing

54   materials (Lack and Cappa, 2010) during atmospheric aging. The coating materials can focus more light onto

55   the soot core through the lensing effect, resulting in elevated MAE (Wang et al., 2017). Strong correlations

56   between MAE and the number fraction of coated particles have been reported in urban areas in China like

57   Shenzhen (Lan et al., 2013) and Xi'an (Wang et al., 2014), implying that the elevated MAE observed at these

58   locations was mainly due to the elevated fraction of coated of soot particles. Total absorption ($\sigma_{abs,t}$) of coated

59   particles can be separated into two parts: primary absorption ($\sigma_{abs,p}$) due to the uncoated soot core alone, and

60   extra absorption ($\sigma_{abs,c}$) due to lensing effect of the coating and the presence of secondarily formed brown

61   carbon (BrC).

62
$$\sigma_{abs,t} = \sigma_{abs,p} + \sigma_{abs,c} \tag{2}$$

63   The absorption enhancement factor (E_{abs}) then can be defined as ratio of the total absorption and primary

64   absorption coefficients or the corresponding MAE values:

65
$$E_{abs} = \frac{\sigma_{abs,t}}{\sigma_{abs,p}} = \frac{MAE_t}{MAE_p} \tag{3}$$

66   Where MAE_p represents the ratio of $\sigma_{abs,p}/EC$ for uncoated soot particles, similar to the concept of the

67   primary OC/EC ratio in the EC tracer method:

68
$$MAE_p = \frac{\sigma_{abs,p}}{EC} \tag{4}$$

69   And the MAE of coated BC can be defined as:

70
$$MAE_t = \frac{\sigma_{abs,t}}{EC} \tag{5}$$

71   Thus, elevated MAE induced by coating during atmospheric aging results in an E_{abs} larger than 1.

72   Previous model studies suggest that absorption by aged soot particles can be 1.5 times greater than fresh soot

73   (Fuller et al., 1999;Bond et al., 2006). Laboratory studies have demonstrated that soot particles coated with

74   SOA (Saathoff et al., 2003;Schnaiter et al., 2005) and sulfuric acid (Zhang et al., 2008;Khalizov et al., 2009)

75   can increase E_{abs}. An artificial coating experiment by Shiraiwa et al. (2010) found an E_{abs} of 2 for graphite

76   particles growing in diameter from 185 to 370 nm. A recent chamber study coupling actual ambient air with

77   seed BC particles implies that the timescale for E_{abs} reaching 2.4 is only 5 hours in Beijing but 18 hours in

78   Houston (Peng et al., 2016). Field studies conducted in recent years have also substantiated enhanced light

79   absorption in Canada (Knox et al., 2009;Chan et al., 2011), US (Lack et al., 2012b), UK (Liu et al., 2015) and

80   Japan (Nakayama et al., 2014;Ueda et al., 2016). A recent study suggests the mass ratio of non-BC content to

81   BC particles determines the occurrence of the absorption enhancement of black-carbon particles (Liu et al.,

82   2017).

83   Two approaches are widely used to determine E_{abs} from ambient measurements. The first approach

84   removes the coating materials on particles physically using a thermal denuder (TD) (Lack et al., 2012a) or by

85   aerosol filter filtration-dissolution (AFD) (Cui et al., 2016b). The TD is briefly discussed here. Coating

86   materials can be removed by TD at a working temperature around 200 to 300 °C (depending on the charring

87   characteristics of aerosols at the sampling site) to measure $\sigma_{abs,p}$, which are cycled with measurements of

88   $\sigma_{abs,t}$ (without passing through TD), allowing E_{abs} to be obtained from the ratio of $\sigma_{abs,t}/\sigma_{abs,p}$ following

89   Eq.3. The major advantage of the TD approach is its ability to provide highly time resolved measurements

90   (minutes). A photo-acoustic spectrometer (PAS) is commonly used with TD for detection to satisfy its high

91   time resolution demands. One limitation of the TD approach is that a universal optimal operation temperature

92   does not exist. If the temperature is too low, the coating cannot be fully removed, and charring can occur if

93   the TD temperature is too high, leading to biased results. Another issue is particle loss due to TD, which can

94   be ~ 20% and needs to be taken into account (Ueda et al., 2016).

95   The second approach is the MAE ratio method, which is also stated in Eq. 3. The key to this method is

96   determining an appropriate MAE_p that can represent the MAE from primary emissions. One approach is to

97   adopt the reference MAE_p from the literature but it may fail to represent the actual MAE_p at a specific sampling

98   site, since MAE_p varies temporally and spatially. The other commonly used approach is to determine MAE_p

99   from the dependency of MAE on the number fraction of coated soot particles measured by SP2 (Lan et al.,

100 2013). Since MAE (y axis) is positively correlated with the number fraction of coated soot particles (x axis),

101 MAE_p can be determined by extending the regression line to x=0.

102   However, the high cost of the TD-PAS system and SP2 limit the field measurement of E_{abs} around the

103 world. In addition, long-term E_{abs} measurements by a TD-PAS system and SP2 are not easily achieved and

104 rarely reported. On the other hand, an Aethalometer and RT-ECOC analyzer can be effectively deployed for

105 long term measurements and E_{abs} estimation, at a relatively lower cost. In this study, based on one year of

106 hourly MAE measurements (with the field carbon analyzer and Aethalometer) at a suburban site in the Pearl

107 River Delta (PRD) region of China, quantification of MAE_p is demonstrated by a novel statistical approach,

108 the Minimum R squared method (MRS) (Wu and Yu, 2016). The aim of this study is to demonstrate the

109 capability of E_{abs} estimation using a year-long dataset from cost-effective instrumentation. The seasonal

110 variability of MAE, AAE and E_{abs} in the PRD region are characterized and their dependency on air mass

111 origin, biomass burning and RH are discussed. Abbreviations used in this study are summarized in Table 1

112 for a quick lookup.

2 Ambient measurements

Sampling was conducted from Feb 2012 to Jan 2013 at the suburban Nancun (NC) site (23° 0'11.82"N, 113°21'18.04"E). NC, situated on the top of the highest peak (141 m ASL) in Guangzhou's Panyu district, is located at the geographic center of the PRD region, making it a representative location for average atmospheric mixing characteristics of city clusters in the PRD region. Light absorption measurements were performed by a 7-λ Aethalometer (AE-31, Magee Scientific Company, Berkeley, CA, USA). Light scattering was measured by an integrating nephlometer (Aurora-1000, Ecotech, Melbourne, Australia). Water soluble ions were measured by MARGA (The instrument for Measuring AeRosols and GAses)(ten Brink et al., 2007). EC mass concentrations were determined by a real time ECOC analyzer (Model RT-4, Sunset Laboratory Inc., Tigard, Oregon, USA). The Aethalometer was equipped with a 2.5 μm cyclone with a sampling flow rate of 4 L min^{-1}. Weingartner's algorithm (Weingartner et al., 2003) was adopted to correct the sampling artifacts (aerosol loading, filter matrix and scattering effect) rooted in filter based method. A customized Aethalometer data processing program (Wu, 2017a) with graphical user interface was developed to perform data correction and detailed descriptions can be found in the SI (The program is available from https://sites.google.com/site/wuchengust). Details of the Aethalometer setup and data correction can be found in our previous paper (Wu et al., 2013). The sunset carbon analyzer was sampling on hourly cycles at a flow rate of 8 Lmin^{-1} with a PM$_{2.5}$ sharp-cut cyclone inlet. For each measurement hour, the first 45min were for sample collection and the remaining 15 min for thermal-optical analysis. OC is volatized first by step-wise temperature ramping in an oxygen-free atmosphere while in the second stage EC is combusted in the presence of oxygen. Laser transmittance is applied to correct the charring artifact during the OC stage.

Considering a measurement uncertainty of 5% for the Aethalometer(Hansen, 2005) and 24% for the RT-ECOC analyzer (Bauer et al., 2009), the propagated relative uncertainty of E$_{abs}$ ($E_{abs,Unc}$) is 35% following Eq. S1&S2 in the SI. It should be noted that $E_{abs,Unc}$ is mainly attributed to the measurement uncertainty of EC by the RT-ECOC analyzer. Since the measurement uncertainty of the RT-ECOC analyzer estimated by Bauer et al. (2009) is obtained from field measurement at an environment (EC below 1 μg m^{-3}) where EC is much lower than the present study (annual average EC 2.63 μg m^{-3}), the $E_{abs,Unc}$ of 35% should be considered as an upper limit for the present study.

2.1 Uncertainties of MAE determination

140

141   Two major uncertainties associated with the σ_{abs} and EC determination techniques should be taken

142 into account when comparing MAE across different studies. For the σ_{abs} determination technique, photo-

143 acoustic spectroscopy (PAS) is an in-situ technique free from filter based artifacts, but its application is limited

144 by its high cost. The filter based optical transmittance method (e.g., Aethalometer and Multi Angle Absorption

145 Photometer, MAAP) is the most widely used technique around the world, but data correction is needed to

146 minimize the bias from artifacts due to the loading effect, matrix effect and scattering effect (Coen et al.,

147 2010). In our study, careful corrective measures (Wu et al., 2013) are conducted for the Aethalometer σ_{abs}

148 data treatment to minimize these artifacts. But such artifacts still cannot be fully eliminated.

149   For the EC determination, different thermal optical analysis (TOA) protocols can impact the

150 measurement variability and thus MAE. As shown in Table S1, MAE for the same samples at Fresno varied

151 from 6.1 to 9.3 $m^2\,g^{-1}$, depending on which EC analysis protocol was applied (Chow et al., 2009). Studies in

152 the PRD found that discrepancies in measured EC by different analysis protocols could be as large as a factor

153 of 5 (Wu et al., 2012;Wu et al., 2016a), which adds to the uncertainty for the MAE estimation. In addition,

154 EC by TOA is also different from refractory BC (rBC) reported by the laser induced incandescence (LII)

155 technique (e.g. single particle soot photometer, SP2). For example, two studies in Toronto (Knox et al.,

156 2009;Chan et al., 2011) both used the PAS for σ_{abs} measurement but different techniques for EC mass

157 determination, resulting in very different MAE results. LII instruments are usually calibrated with a

158 commercially available surrogate (e.g. fullerene) since direct calibration with ambient soot is not easy to

159 achieve. Laborde et al. (2012) indicates that the incandescence response of SP2 exhibits a dependency on soot

160 type (15% between fullerene and denuded diesel soot particles; 14% between biomass burning and denuded

161 diesel soot particles). Due to the absence of widely accepted reference materials for EC, the uncertainties in

162 EC determination will exist in the foreseeable future. All these uncertainties, including the uncertainty of rBC

163 mass determination by SP2, uncertainty of EC in TOA, the discrepancy between SP2 rBC and TOA EC and

164 the discrepancy of σ_{abs} between filter transmission and photo-acoustic methods, can contribute to the

165 differences in MAE listed in Table S1.

166   It is worth noting that MAE uncertainties (e.g. uncertainties of σ_{abs} and variability of EC mass by

167 different TOA protocols) discussed above have little effect on E$_{abs}$ estimation. As shown in Eq. 3, E$_{abs}$ is the

Atmospheric
Chemistry
and Physics
Discussions

168   ratio of MAE_t to MAE_p or $\sigma_{abs,t}$ to $\sigma_{abs,p}$, thus most of the bias in EC mass or σ_{abs} is cancelled out during

169   the E_abs calculation.

3 Methodology

3.1 MAE_p estimation by MRS from the ambient data

172   In this section, a new approach for MAE_p estimation is introduced for E_abs determination, which requires the

173   knowledge of differentiating $\sigma_{abs,p}$ and $\sigma_{abs,c}$ portions in $\sigma_{abs,t}$. The idea of decoupling $\sigma_{abs,t}$ into

174   $\sigma_{abs,p}$ and $\sigma_{abs,c}$ is conceptually similar to decoupling OC into primary OC (POC) and secondary OC (SOC)

175   in the EC tracer method as shown in Table 2. In the EC tracer method, if (OC/EC)_p is known, POC can be

176   determined from OC (Turpin and Huntzicker, 1991). The role of MAE_p here is similar to the role of (OC/EC)_p,

177   the primary OC/EC ratio in the EC tracer method (a comparison is given in Table 2). If MAE_p (average MAE

178   from primary emission sources) is known, E_abs can be obtained from the ratio of MAE_t/MAE_p (Eq. 3).

179   Therefore, the key for E_abs estimation is to derive an appropriate MAE_p. It is worth noting that MAE_p here

180   does not represent MAE from a single or specific primary emission source, instead it reflects an average and

181   effective MAE that has taken consideration of various primary emission sources. Thus, the MAE_p is

182   conceptually analogous to (OC/EC)_p in the EC tracer method, in which the primary ratio reflects an overall

183   ratio from primary emission sources rather than from a single primary source.

184   The Minimum R squared method (MRS) explores the inherent independency between pollutants from

185   primary emissions (e.g., EC) and products associated with secondary formation processes (e.g., SOC, $\sigma_{abs,c}$)

186   to derive the primary ratios (e.g., (OC/EC)_P, MAE_p) in the EC tracer method(Wu and Yu, 2016). When

187   applying MRS for light absorption enhancement estimation, MRS is used to explore the inherent independency

188   between EC and $\sigma_{abs,c}$, which is gained during atmospheric aging after emission. An example of MAE_p

189   estimation by MRS is shown in Figure 1. Firstly, the assumed MAE_p value is varied continuously in a

190   reasonable range (0.01 to 50 $m^2\ g^{-1}$ as shown in Figure 1). Then at each hypothetical MAE_p, $\sigma_{abs,c}$ can be

191   calculated by Eq. 6 (a combination of Eq. 2&4) using EC and $\sigma_{abs,t}$ from ambient measurements.

$$\sigma_{abs,c} = \sigma_{abs,t} - MAE_p \times EC \tag{6}$$

193   Accordingly, for each hypothetical MAE_p, a correlation coefficient value (R^2) of $\sigma_{abs,c}$ vs. EC (i.e.,

194   $R^2(\sigma_{abs,c}, EC)$) can be obtained. The series of $R^2(\sigma_{abs,c}, EC)$ values (y axis) are then plotted against the

195   assumed MAE$_p$ values (x axis) as shown by the red curve in Figure 1. The physical meaning of this plot can

196   be interpreted as follows. The $\sigma_{abs,p}$ is the fraction of light absorption owing to primary emitted soot particles.

197   As a result, $\sigma_{abs,p}$ is well correlated with EC mass. In contrast, the $\sigma_{abs,c}$ is the fraction of light absorption

198   gained by the lensing effect of the coating on particles after emission. The variability of $\sigma_{abs,c}$ mainly

199   depends on the coating thickness of the soot particles. Consequently, $\sigma_{abs,c}$ is independent of EC mass. Since

200   variations of EC and $\sigma_{abs,c}$ are independent, the assumed MAE$_p$ corresponding to the minimum

201   R^2(EC, $\sigma_{abs,c}$) would then represent the most statistically probable MAE$_p$ of the tested dataset.

202   A computer program (Wu, 2017b) in Igor Pro (WaveMetrics, Inc. Lake Oswego, OR, USA) was

203   developed to facilitate MRS calculation with a user friendly graphical user interface. Another two Igor Pro

204   based computer programs Histbox (Wu, 2017c) and Scatter Plot (Wu, 2017d) are used for generating

205   histograms, box plots and scatter plots (with Deming regressions) presented in this study. Detailed descriptions

206   of these computer programs can be found in the SI and the computer programs are available from

207   https://sites.google.com/site/wuchengust.

3.2 Mie simulation

209   It can be informative to model a single soot particle using Mie theory (Bohren and Huffman, 1983)

210   and understand the theoretical range and variability of the soot particle's optical properties. Three types of

211   mixing state are widely employed for parameterization: internal mixing, external mixing and core-shell. To

212   better represent the real situation (coating due to the aging process), a core-shell model is considered in the

213   Mie calculation (Figure 2), which is more realistic than a volume mixture model (Bond et al., 2006). An

214   aerosol optical closure study in the North China Plain (NCP) found that the core-shell model can provide

215   better performance than assuming purely internal mixing and external mixing (Ma et al., 2012). A morphology

216   study using Scanning Transmission X-ray Microscopy found that core-shell is the dominating mixing state in

217   ambient samples (Moffet et al., 2016). It should be noted that the core-shell model assumption still has its own

218   limitations. A single particle soot photometer (SP2) study by Sedlacek et al. (2012) reported a negative lag

219   time between the scattering and incandescence signals in samples influenced by biomass burning, implying

220   a near surface location of soot relative to non-absorbing materials. Near surface type mixing of soot has also

221   been observed in Tokyo, but accounted for only 10% of total mixed soot containing particles (Moteki et al.,

Atmospheric
Chemistry
and Physics
Discussions

222   2014). Considering the domination of core-shell type particles in the ambient environment, the core-shell

223   assumption in our optical model is sufficient to approximate the real situation.

224   As shown in Figure 2, fresh emitted soot particles are chain-like aggregates of small spheres (30~50

225   nm). After the aging process, soot particles are coated with organic and inorganic materials. Sufficient

226   evidence has shown that the coating not only results in particle size growth, but also makes the soot core

227   become more compact due to its collapse (Alexander et al., 2008;Zhang et al., 2008;Lewis et al., 2009). Since

228   the spherical like core and shell favor Mie simulation, both core and shell are considered as spheres in the Mie

229   calculation.

230   To investigate the spectrum properties of soot particles, 11 wavelengths (370, 405, 470, 520, 532, 550,

231   590, 660, 781, 880 and 950 nm) are considered in calculations to cover wavelengths in the most frequently

232   used absorption measurement instruments. A refractive index (RI) of $1.85 - 0.71i$ is adopted for soot core

233   (Bond and Bergstrom, 2006) and 1.55 for non-absorbing coating (clear shell) in the Mie calculation for all

234   wavelengths. Studies suggest a group of organic matter (OM), known as Brown Carbon (BrC), can absorb

235   solar radiation at UV wavelengths (Kirchstetter et al., 2004). Thus, a BrC coating (brown shell) scenario is

236   also considered in Mie simulation following the wavelength dependent RI suggested by Lack and Cappa

237   (2010). A modeling study by Bond et al. (2006) indicates that absorption amplification is not sensitive to the

238   RI, thus the result below is not expected to be sensitive to the RI variability. Both core diameters (D_{core}) and

239   shell diameters (D_{shell}) are constrained in the range of 10 ~ 3000 nm in the model simulations. The Mie

240   calculations are implemented with a customized program (Wu, 2017e) written in Igro Pro (WaveMetrics, Inc.

241   Lake Oswego, OR, USA) and it is available from https://sites.google.com/site/wuchengust. It should be noted

242   that the core-shell type mixing state of particles is still rare in 3D atmospheric models like WRF-Chem (Matsui

243   et al., 2013;Nordmann et al., 2014) due to computational cost limitation.

244   **3.2.1 Absorption Angstrom Exponent (AAE)**

245   Absorption Angstrom Exponent (AAE) is a widely used parameter that describes the wavelength

246   dependence of aerosol light absorption (Moosmuller et al., 2011), which can be written explicitly as

247    $$AAE(\lambda_1, \lambda_2) = -\frac{\ln(\sigma_{abs,\lambda 1}) - \ln(\sigma_{abs,\lambda 2})}{\ln(\lambda_1) - \ln(\lambda_2)} \tag{7}$$

248   It is well known that ambient soot particles exhibit an AAE close to unity (Bond, 2001). Modeled

249   variability in $AAE_{470-660}$ of bare soot particles is shown in Figure S1. For soot particles with D_{core} <200 nm,

250    $AAE_{470-660}$ is very close to 1 and decreases significantly for particles with D_{core} >200 nm. Considering a typical

251   D_{core} of fresh emitted soot particles smaller than 200 nm (Rose et al., 2006;China et al., 2013), the model

252   results confirm the frequently observed AAE close to 1 from ambient measurements (Kirchstetter et al., 2004).

253   Modeled variability in $AAE_{470-660}$ of soot particles coated by non-absorbing substances (clear shell) and

254   weakly absorbing materials (brown shell) is shown in Figure 3. Elevated AAE to ~2 is observed in the clear

255   shell scenario (Figure 3a and 3b) for the most probable soot core particle sizes (<200 nm), which agrees well

256   with a previous model study (Lack and Cappa, 2010), implying that elevated AAE cannot be exclusively

257   attributed to mixing with BrC. AAE elevation is more pronounced in the brown shell scenario. For soot

258   particles with D_{core} <200 nm, brown shell $AAE_{470-660}$ can easily reach 3 for a coating of D_{shell}/D_{core}=3 (Figure

259   3c and 3d). These high AAE results are consistent with previous model studies (Lack and Cappa, 2010) and

260   measurement studies (Kirchstetter et al., 2004;Hoffer et al., 2006).

261   **3.2.2 Single scattering albedo (SSA)**

262   Variability in modeled SSA of soot particles coated by non-absorbing substances and weakly

263   absorbing materials (e.g. BrC) is shown in Figure S2. For particles with D_{core}<200 nm and D_{shell}/D_{core} <3, the

264   SSA increases gradually (up to ~0.9) with a thicker coating and behaves similarly between clear shell and

265   brown shell scenarios.

266   **3.2.3 Mass absorption efficiency (MAE)**

267   MAE is a useful indicator for soot mixing state. Variability in MAE of bare soot particles as a function

268   of particle size at a wavelength of 550nm is illustrated in Figure S3. The magnitude of MAE is sensitive to

269   the soot density assumption, especially for particles <200 nm (Figure S3), but the overall trend of particle size

270   dependency is similar between different density scenarios. MAE peaks at a particle size of 200 nm and

271   decreases dramatically for larger particles. In our MAE calculation, a soot density of 1.9 g cm^{-3} is adopted, as

272   suggested by Bond and Bergstrom (2006). The purpose of adopting constant density is to simplify the MAE

273   calculation. It should be noted that the effective density of soot core is highly variable in ambient environments.

274   For example, a study in Beijing (Zhang et al., 2016b) found a value of 1.2 g cm^{-3}. A recent chamber study

Atmospheric
Chemistry
and Physics
Discussions

Open Access

275   found the effective density of soot can evolve from 0.43 to 1.45 g cm^{-3} during aging as coated by m-Xylene

276   oxidation products (Guo et al., 2016). A study by a single-particle aerosol mass spectrometer in Guangzhou

277   found the effective density of soot increased with particle size in the range of 400 to 1600 nm(Zhang et al.,

278   2016a). The MAE of coated particles from different core/shell diameter combinations are shown in Figure S4.

279   For thickly coated particles, the MAE in the clear shell scenario varied as D_{shell}/D_{core} increased, but the MAE

280   of brown shell scenario increased quasi-monotonously with D_{shell}/D_{core}.

3.2.4 Light absorption enhancement factor (E_{abs})

282   E_{abs} is a better indicator for soot mixing state than MAE since it does not rely on the soot density

283   assumption and is more suitable for comparing Mie simulations with ambient measurements. Modeled

284   variability in E_{abs} of soot particles coated by non-absorbing substances and weakly absorbing materials (e.g.

285   BrC) is shown in Figure 4a and 3c respectively. E_{abs} is not only sensitive to the core/shell diameter combination,

286   but also behaves very differently on the clear and brown shell assumptions. For the clear shell scenario, when

287    $D_{coat}/D_{core} < 2$, E_{abs} does not exceed 2 for particles with different soot core sizes, but for the same D_{coat}/D_{core}, a

288   larger soot core size yields a higher E_{abs} (Figure 4b, cross-sections of Figure 4a). If $D_{coat}/D_{core} > 2$, E_{abs} could

289   be 3 to 5 for particles with a soot core smaller than 200 nm, but for particles with a soot core larger than 200

290   nm, the E_{abs} is limited to ~2 as shown in Figure 4b. For the brown shell scenario, E_{abs} increased quasi-

291   monotonically with D_{coat}/D_{core}, and this trend is similar for different soot core sizes (Figure 4d). Another major

292   difference between the clear and brown shell scenarios is that, for thickly coated particles (e.g. $D_{coat}/D_{core} > 2$),

293   the brown shell can yield a much higher E_{abs} than the clear shell.

294   Both primary soot size distribution and coating thickness can affect the absorption enhancement of

295   ambient BC particles. Ambient measurements by LII found soot particle number and mass concentrations

296   peaking at 110 nm and 220 nm, respectively, in the PRD (Huang et al., 2011b). A study in Shanghai found

297   similar results (70 nm for number concentrations and 200 nm for mass concentrations)(Gong et al., 2016).

298   Considering that the LII technique is specific for BC mass determination which is independent of BC mixing

299   state, the size distribution reported by LII can represent the size distribution of the BC core. A study using a

300   Micro Orifice Uniform Deposit Impactor (MOUDI) found a EC mass size distribution in the PRD exhibiting

301   three modes peaking at ~300, ~900 and ~5000 nm (Yu et al., 2010), implying a substantial coating of BC

302   particles, and a diameter amplification of 3. A recent closure study on BC mixing state in the PRD region

Atmospheric
Chemistry
and Physics
Discussions

303   suggests σ_{abs} is dominated by soot particles in the range of 300~400 nm (Tan et al., 2016). Considering the

304   dominant BC core distribution measured by SP2 (110 nm), the upper limit of E_{abs} in the PRD is roughly

305   estimated as ~2 for the clear shell scenario (Figure 4b).

4 Results and discussions

4.1 Annual measurement statistics

308   The frequency distribution (log-normal) of σ_{abs550} is shown in Figure 5a, with an annual average (±1

309   S.D.) of 42.20±30.81 Mm^{-1}. A log-normal distribution is also found in the EC mass concentration (Figure 5b),

310   with an annual average of 2.63±2.27 µg m^{-3}. Figure 5c demonstrates the yearlong frequency distribution of

311   MAE$_{550}$ at the NC site. The annual average MAE$_{550}$ is 19.02±6.60 m^2 g^{-1} and peaks (±1 S.D.) of the normal

312   and lognormal fits are 16.16±4.57 and 15.70±0.22 m^2 g^{-1} respectively. A good correlation is observed between

313   σ_{abs} and EC mass (R^2=0.92) as shown in Figure 5d, and the color coding indicates a MAE dependency on

314   RH (the RH effect will be discussed in section 4.5). Annual average AAE$_{470-660}$ is 1.08±0.12 (Figure S5a),

315   indicating that soot is the dominant absorbing substance in the PRD and the brown shell scenario shown in

316   the Mie simulation is unlikely to be important. Annual mean SSA is 0.86±0.05 (Figure S5b), similar to

317   previous studies in the PRD (Jung et al., 2009;Wu et al., 2009). As shown in Table S1, MAE$_{550}$ by previous

318   studies was found to cover a wide range, from 5.9 to 61.6 m^2 g^{-1}. Annual average observed MAE at NC (19.02

319   m^2 g^{-1}) is higher than many studies shown in Figure 6, e.g., Shenzhen (Lan et al., 2013), Beijing (Yang et al.,

320   2009) and Mexico city (Doran et al., 2007).

321   As shown in Figure 1, the annual average MAE$_p$ estimated by MRS is 13 m^2 g^{-1}. The estimated MAE$_p$

322   is higher than Guangzhou (7.44 m^2 g^{-1}) (Andreae et al., 2008), but comparable to Xi'an (11.34 m^2 g^{-1}) (Wang

323   et al., 2014), Toronto (9.53~12.57 m^2 g^{-1}) (Knox et al., 2009) and a rural Mediterranean site (12.04 m^2 g^{-1})

324   (Pandolfi et al., 2011). The annual average E_{abs} by MRS following Eq. 3 is estimated to be 1.52.

325   It should be noted that the E_{abs} estimation approach demonstrated here is not affected by the MAE bias

326   (e.g. overestimation of σ_{abs} and variability of EC mass by different TOA protocols) discussed in section 2.1,

327   because bias in EC mass or σ_{abs} is cancelled out in the E_{abs} calculation (Eq. 3), since E_{abs} is the ratio of $\sigma_{abs,t}$

328   to $\sigma_{abs,p}$. The E_{abs} could vary by location, depending on the coating thickness and size distribution of the

329   primary aerosols. After undergoing atmospheric aging, the E_{abs} can be increased during transport from

Atmospheric
Chemistry
and Physics
Discussions

330   emission source to rural areas. The magnitude of the E_{abs} found at the NC site is comparable to other locations

331   such as Boulder (Lack et al., 2012a) (1.38), London (Liu et al., 2015) (1.4), Shenzhen (Lan et al., 2013) (1.3),

332   Yuncheng (Cui et al., 2016b) (2.25), Jinan (Chen et al., 2017) (2.07) and Nanjing (Cui et al., 2016a) (1.6), as

333   listed in Table 3. Spectrum E_{abs} are calculated from 370 to 950 nm as shown in Figure S6. E_{abs} in the PRD

334   exhibits a weak wavelength dependence, with slightly higher E_{abs} at the shorter wavelength (e.g. $E_{abs370} = 1.57$)

335   and is relatively lower in the IR range (e.g. $E_{abs950} = 1.51$).

4.2 Monthly characteristics of MAE, AAE and SSA

337   Monthly variations of MAE_{550} at the NC site are shown in Figure 7a and Table S2, revealing distinct patterns

338   of higher MAE_{550} in summer and lower in winter. On the other hand, $AAE_{470-660}$ is lower in summer and

339   higher in winter (Figure 7b and Table S3). Monthly SSA varied from 0.83 to 0.90 without a clear seasonal

340   pattern, as shown in Figure S7 and Table S4. MAE_p estimation for individual months is shown in Figure 7a

341   and monthly E_{abs550} is calculated accordingly following Eq. 3 (Figure 7c). E_{abs550} shows clear seasonal

342   variations, with higher values from April to August (1.5~1.97 as shown in Table S5) and relatively lower

343   values from September to March (1.17~1.47). The highest enhancement is found in August (1.97). Factors

344   affecting variation of E_{abs} are discussed in the following sections, including air mass origin, biomass burning

345   and RH.

4.3 The effect of air mass origin

347   It's of interest to understand the seasonal variations of optical properties in the PRD. Hourly backward

348   trajectories for the past 72 hours were calculated using NOAA's HYSPLIT (Hybrid Single Particle Lagrangian

349   Integrated Trajectory, version 4) model (Draxier and Hess, 1998) from Feb 2012 to Jan 2013 as shown in

350   Figure S8. Cluster analysis was conducted using MeteoInfo (Wang, 2014). By examining the total spatial

351   variance (TSV), the number of clusters was determined to be four as shown in Figure S9. Cluster 1 (C1)

352   represents continental air masses from the north, accounting for 44.4% of total trajectories. C2 (22.8%)

353   represents marine air masses coming from the South China Sea. C3 represents air masses from the east

354   (Taiwan island). C4 (15.8%) represents transitional air masses coming from the east coastline of China. As

355   shown in Figure 8, E_{abs550} from C2 (1.78) is significantly higher than other clusters (1.30 – 1.42), implying

356   that particles from the South China Sea cluster is likely more aged than other clusters. Air mass origin in the

Atmospheric
Chemistry
and Physics
Discussions

357   PRD is dominated by C2 from Apr to Aug (Figure S10a) as a result of the South China Sea monsoon in the

358   rainy season. In contrast, the dry season is ruled by continental air masses from the north (C1) due to the

359   influence of the northeast monsoon. E_{abs550} from C2 varied from 1.67 to 2.19, but was always higher than

360   E_{abs550} from C1 and C3 during the rainy season (Figure S10b). As a result, the domination of aged air mass

361   from the vast ocean is one of the reasons for the much higher E_{abs550} found in the rainy season.

362   **4.4 The effect of biomass burning**

363   Biomass burning (BB) and vehicular emission are the two major sources of soot particles. BC from

364   biomass burning emission, depending on the fuel type and burning condition, may have a higher OC/EC ratio

365   and a thicker coating, resulting in a higher MAE than vehicular emission (Shen et al., 2013;Cheng et al., 2016) .

366   In this study, the influence of BB on optical properties is investigated using the K^+/EC ratio as a BB indicator.

367   As shown in Figure 9, MAE_{550} is positively correlated with the K^+/EC ratio, which exhibits a clear seasonal

368   pattern that is higher in the rainy season and lower in the dry season (Figure S11). Southeast Asia has the

369   highest fire emission density globally due to the high biofuel consumption along with frequent fire activity in

370   this region (Aouizerats et al., 2015), making Southeast Asia a large contributor to BC emissions (Jason Blake,

371   2014). During the rainy season when oceanic prevailing wind dominates, BC from BB emission in Southeast

372   Asia can reach PRD through long range transport (LRT), resulting in an elevated K^+/EC ratio and MAE_{550},

373   which might be a combination of a thicker coating when freshly emitted from BB sources and enhanced

374   coating during LRT. The Deming regression intercept (11.89) in Figure 9 represents MAE without a BB effect.

375   This non-BB MAE_{550} (11.89 $m^2\,g^{-1}$) is lower than MAE_p (13 $m^2\,g^{-1}$) obtained in section 4.3, implying that BB

376   is an ubiquitous source of BC in the PRD region.

377   Many studies have found that BB influenced samples exhibit elevated AAE due to the presence of

378   wavelength dependent light absorbing substances like BrC and HUmic-LIke Substances (HULIS)(Kirchstetter

379   et al., 2004;Hoffer et al., 2006;Sandradewi et al., 2008;Herich et al., 2011;Pokhrel et al., 2017). It is of interest

380   to investigate whether elevated AAE observed in the PRD during the dry season is associated with BB

381   influence. As shown in Figure S12, $AAE_{370-470}$ and $AAE_{470-660}$ didn't correlate with the BB indicator, K^+/EC

382   ratio. These results suggested that elevated AAE observed in the PRD wintertime is unlikely to be dominated

383   by BrC. As discussed in our Mie simulation (section 3.1) and a previous study (Lack and Cappa, 2010), coating

384   of non-absorbing materials onto soot particles can increase AAE up to 2. Since the monthly average AAE in

Atmospheric
Chemistry
and Physics
Discussions

385 wintertime didn't exceed 1.2 (Table S3), the variations of AAE in the PRD are likely more associated with

386 thicker coatings rather than the contribution of BrC. The results also imply that attempts on BrC absorption

387 attribution for the PRD dataset presented in this study could be risky, considering that elevation of AAE is

388 actually dominated by coating (Lack and Langridge, 2013).

4.5 The effect of relative humidity (RH) on optical properties

390 Soot particles are relatively hydrophobic when freshly emitted, but tend to gain hygroscopicity during

391 atmospheric aging. Hygroscopic growth of coated laboratory generated model BC was reported by

392 McMeeking et al. (2011). Growth of ambient BC particle size by a factor of 1.4-1.6 under high RH has been

393 observed in a UK study (Liu et al., 2013). Located in the subtropical zone, RH plays an important role on

394 aerosol optical properties in the PRD region. The yearlong measurements at the NC site provide a unique

395 opportunity to investigate the effect of RH on aerosol optical properties, since most existing ad hoc studies in

396 the PRD only last for months. Liquid water content (LWC) was calculated using the E-AIM (model 2)

397 thermodynamic model (Clegg et al., 1998). As shown in Figure S13, LWC on average accounted for a

398 significant fraction (44%) of non-EC $PM_{2.5}$ mass, making it an important component of $PM_{2.5}$ mass and due

399 to high RH in the PRD. Previously, hygroscopic growth was only considered for particle scattering in the

400 IMPROVE formula for chemically resolved light extinction budget studies. In this study f(RH) of MAE was

401 obtained from yearlong measurements as shown in Figure 10a for RH = 30 ~100% and color coded for LWC.

402 It clearly shows that MAE_{550} measured in NC is positively correlated with RH and the enhancement can be

403 fitted by a polynomial equation. When RH is close to 100%, the LWC can account for 70% of $PM_{2.5}$ mass.

404 The maximum f(RH) can reach 1.3, which is higher than the value found in Beijing (1.2) (Wu et al., 2016b).

405 These results reveal that a large contribution of E_{abs} is coming from high LWC under high RH in the PRD

406 region. Because RH has a clear diurnal pattern, it can affect the diurnal pattern of E_{abs} in the PRD. Since the

407 RH effect on E_{abs} is rarely considered in existing climate models, the inclusion of RH effect can reduce the

408 uncertainty for assessing BC's climate effect.

409 The $AAE_{470-660}$ dependency on RH is shown in Figure 10b. When RH is low (e.g. 30%), the $AAE_{470-660}$ is around 1.25 and decreases to 1.10 as RH increases to 50%. $AAE_{470-660}$ remains around 1.12 when RH is

411 50-70%. Then $AAE_{470-660}$ decreases again when RH is higher than 70% and can reach 1 when RH is close to

412 100%. Since a higher RH results in hygroscopic growth and larger particle diameters, the negative correlation

413 between $AAE_{470-660}$ and RH provides a clue on soot particles' primary diameter and mixing state. As shown

414 in the Mie simulation in Figure 3b, for a particle with D_{core} of 130 nm and D_{shell}/D_{core} of 2 to 4, $AAE_{470-660}$

415 decreases as the coating increases, and the decrease tapers off when $D_{shell}/D_{core} = 3$. The D_{core} obtained here

416 (130nm) is comparable with D_{core} obtained from SP2 measurements (110nm) in the PRD (Huang et al., 2011a).

4.6 Implications for mixing state

418 Quantitative direct measurements of BC mixing state and coating thickness are still challenging. SP2

419 can estimate the coating thickness using a lag-time approach or a Mie calculation approach can be employed,

420 but both methods have a limited range in coating thickness and uncertainties arise from the assumptions made

421 during the retrieval. For example, recent studies found that the mass equivalent diameter of soot core measured

422 by SP2 could be underestimated due to density assumptions (Zhang et al., 2016b). Although size distribution

423 measurement is not available in this study, clues of mixing state still can be derived from bulk measurements

424 of optical properties. As discussed in section 4.4.1, elevated E_{abs} observed in the rainy season is associated

425 with aged air masses from a marine origin. To probe the possible mixing state difference between dry and

426 rainy season, E_{abs550} and $AAE_{470-660}$ are used to narrow down the possible core-shell size range as shown in

427 Figure S14. Monthly averages with one standard deviation of $AAE_{470-660}$ and E_{abs550} are used as constraints to

428 extract the intersecting core-shell size range from Figure 3a and Figure 4a. The results show that March and

429 August have a very different core-shell size range: in March, the core and shell range are 130 ~ 155 nm and

430 140 ~ 250 nm, respectively; in August, the core and shell range are 120 ~ 165 nm and 170 ~ 430 nm,

431 respectively. This confirms again that the soot particles in the rainy season are likely to have a thicker coating

432 than in the dry season.

5 Conclusions

434 In this study, a novel statistical approach is proposed and its application on ambient data is

435 demonstrated using one-year hourly OC and EC data coupled with Aethalometer measurements. Unlike

436 conventional E_{abs} determination approaches that require expensive instrumentation (e.g. TD-PAS, VTDMA,

437 SP2), this new approach employs widely deployed instruments (field carbon analyzer and Aethalometer). The

438 key of this new approach involves calculating MAE_p by the Minimum R Squared (MRS) method (Wu and

439 Yu, 2016). The annual average MAE_p estimated by MRS is 13 m^2 g^{-1} and annual average MAE_{550} is

440   19.02±6.60 $m^2 g^{-1}$, suggesting an annual average enhancement factor (E_{abs}) of 1.52. This value is within the

441   upper limit of E_{abs} (~2) by core-shell Mie simulations considering the typical soot size distribution and coating

442   thickness in the PRD.

443   Both MAE_p and E_{abs} show distinct seasonal variations, implying the complexity of soot particle mixing

444   state variations in this region. The elevated summertime E_{abs} in the PRD is found to be associated with the

445   domination of aged air masses from the South China Sea, along with the long-range transport of biomass

446   burning influenced air masses from Southeast Asia. Hygroscopic growth with elevated RH contributes to E_{abs}

447   as well, which could be as high as 1.3. A negative correlation is found between $AAE_{470-660}$ and RH, suggesting

448   a dominant particle size with a D_{core} of 130 nm and D_{shell}/D_{core} range of 2 to 4. Core-shell size ranges narrowed

449   down by E_{abs550} and $AAE_{470-660}$ constraints suggest that soot particles in the rainy season are likely to have

450   thicker coatings than in the dry season.

451   **Data availability**

452   OC, EC, inorganic ions and σ_{abs} data used in this study are available from corresponding authors upon

453   request.

454

455   **Acknowledgements**

Atmospheric
Chemistry
and Physics
Discussions

Open Access

EGU

Reference

Alexander, D. T. L., Crozier, P. A., and Anderson, J. R.: Brown carbon spheres in East Asian outflow and their optical properties, Science, 321, 833-836, 2008.

Andreae, M. O., Schmid, O., Yang, H., Chand, D., Yu, J. Z., Zeng, L. M., and Zhang, Y. H.: Optical properties and chemical composition of the atmospheric aerosol in urban Guangzhou, China, Atmos. Environ., 42, 6335-6350, doi: 10.1016/j.atmosenv.2008.01.030, 2008.

Aouizerats, B., van der Werf, G. R., Balasubramanian, R., and Betha, R.: Importance of transboundary transport of biomass burning emissions to regional air quality in Southeast Asia during a high fire event, Atmos. Chem. Phys., 15, 363-373, doi: 10.5194/acp-15-363-2015, 2015.

Bauer, J. J., Yu, X.-Y., Cary, R., Laulainen, N., and Berkowitz, C.: Characterization of the Sunset Semi-Continuous Carbon Aerosol Analyzer, J. Air. Waste. Manage., 59, 826-833, doi: 10.3155/1047-3289.59.7.826, 2009.

Bohren, C. F. and Huffman, D. R.: Absorption and scattering of light by small particles, Wiley, New York, xiv, 530 p. pp., 1983.

Bond, T. C.: Spectral dependence of visible light absorption by carbonaceous particles emitted from coal combustion, Geophys.Res.Lett., 28, 4075-4078, doi: Doi 10.1029/2001gl013652, 2001.

Bond, T. C. and Bergstrom, R. W.: Light absorption by carbonaceous particles: An investigative review, Aerosol. Sci. Technol., 40, 27-67, doi: Doi 10.1080/02786820500421521, 2006.

Bond, T. C., Habib, G., and Bergstrom, R. W.: Limitations in the enhancement of visible light absorption due to mixing state, J. Geophys. Res., 111, -, 2006.

Bond, T. C., Zarzycki, C., Flanner, M. G., and Koch, D. M.: Quantifying immediate radiative forcing by black carbon and organic matter with the Specific Forcing Pulse, Atmos. Chem. Phys., 11, 1505-1525, doi: 10.5194/acp-11-1505-2011, 2011.

Cappa, C. D., Onasch, T. B., Massoli, P., Worsnop, D. R., Bates, T. S., Cross, E. S., Davidovits, P., Hakala, J., Hayden, K. L., Jobson, B. T., Kolesar, K. R., Lack, D. A., Lerner, B. M., Li, S.-M., Mellon, D., Nuaaman, I., Olfert, J. S., Petäjä, T., Quinn, P. K., Song, C., Subramanian, R., Williams, E. J., and Zaveri, R. A.: Radiative Absorption Enhancements Due to the Mixing State of Atmospheric Black Carbon, Science, 337, 1078-1081, doi: 10.1126/science.1223447, 2012.

Chan, T. W., Brook, J. R., Smallwood, G. J., and Lu, G.: Time-resolved measurements of black carbon light absorption enhancement in urban and near-urban locations of southern Ontario, Canada, Atmos. Chem. Phys., 11, 10407-10432, 2011.

Chen, B., Bai, Z., Cui, X., Chen, J., Andersson, A., and Gustafsson, Ö.: Light absorption enhancement of black carbon from urban haze in Northern China winter, Environ Pollut, 221, 418-426, doi: https://doi.org/10.1016/j.envpol.2016.12.004, 2017.

Cheng, Y., Engling, G., Moosmüller, H., Arnott, W. P., Chen, L. W. A., Wold, C. E., Hao, W. M., and He, K.-b.: Light absorption by biomass burning source emissions, Atmos. Environ., 127, 347-354, doi: http://dx.doi.org/10.1016/j.atmosenv.2015.12.045, 2016.

China, S., Mazzoleni, C., Gorkowski, K., Aiken, A. C., and Dubey, M. K.: Morphology and mixing state of individual freshly emitted wildfire carbonaceous particles, Nat Commun, 4, doi: 10.1038/ncomms3122, 2013.

Chow, J. C., Watson, J. G., Doraiswamy, P., Chen, L. W. A., Sodeman, D. A., Lowenthal, D. H., Park, K., Arnott, W. P., and Motallebi, N.: Aerosol light absorption, black carbon, and elemental carbon at the Fresno Supersite, California, Atmos Res, 93, 874-887, doi: DOI 10.1016/j.atmosres.2009.04.010, 2009.

Atmospheric
Chemistry
and Physics
Discussions

506 Clegg, S. L., Brimblecombe, P., and Wexler, A. S.: Thermodynamic Model of the System H+−NH4+−SO42-
507 −NO3-−H2O at Tropospheric Temperatures, The Journal of Physical Chemistry A, 102, 2137-2154, doi:
508 10.1021/jp973042r, 1998.

509 Coen, M. C., Weingartner, E., Apituley, A., Ceburnis, D., Fierz-Schmidhauser, R., Flentje, H., Henzing, J. S.,
510 Jennings, S. G., Moerman, M., Petzold, A., Schmid, O., and Baltensperger, U.: Minimizing light absorption
511 measurement artifacts of the Aethalometer: evaluation of five correction algorithms, Atmos. Meas. Tech., 3,
512 457-474, 2010.

513 Cui, F., Chen, M., Ma, Y., Zheng, J., Zhou, Y., Li, S., Qi, L., and Wang, L.: An intensive study on aerosol
514 optical properties and affecting factors in Nanjing, China, Journal of Environmental Sciences, 40, 35-43, doi:
515 http://dx.doi.org/10.1016/j.jes.2015.08.017, 2016a.

516 Cui, X., Wang, X., Yang, L., Chen, B., Chen, J., Andersson, A., and Gustafsson, Ö.: Radiative absorption
517 enhancement from coatings on black carbon aerosols, Sci.Total.Environ., 551, 51-56, doi:
518 http://dx.doi.org/10.1016/j.scitotenv.2016.02.026, 2016b.

519 Ding, A. J., Huang, X., Nie, W., Sun, J. N., Kerminen, V. M., Petäjä, T., Su, H., Cheng, Y. F., Yang, X. Q.,
520 Wang, M. H., Chi, X. G., Wang, J. P., Virkkula, A., Guo, W. D., Yuan, J., Wang, S. Y., Zhang, R. J., Wu, Y.
521 F., Song, Y., Zhu, T., Zilitinkevich, S., Kulmala, M., and Fu, C. B.: Enhanced haze pollution by black carbon
522 in megacities in China, Geophys.Res.Lett., 43, 2873-2879, doi: 10.1002/2016GL067745, 2016.

523 Doran, J. C., Barnard, J. C., Arnott, W. P., Cary, R., Coulter, R., Fast, J. D., Kassianov, E. I., Kleinman, L.,
524 Laulainen, N. S., Martin, T., Paredes-Miranda, G., Pekour, M. S., Shaw, W. J., Smith, D. F., Springston, S.
525 R., and Yu, X. Y.: The T1-T2 study: evolution of aerosol properties downwind of Mexico City, Atmos. Chem.
526 Phys., 7, 1585-1598, doi: 10.5194/acp-7-1585-2007, 2007.

527 Draxier, R. R. and Hess, G. D.: An overview of the HYSPLIT_4 modelling system for trajectories, dispersion
528 and deposition, Aust Meteorol Mag, 47, 295-308, 1998.

529 Fuller, K. A., Malm, W. C., and Kreidenweis, S. M.: Effects of mixing on extinction by carbonaceous particles,
530 J. Geophys. Res., 104, 15941-15954, 1999.

531 Gong, X., Zhang, C., Chen, H., Nizkorodov, S. A., Chen, J., and Yang, X.: Size distribution and mixing state
532 of black carbon particles during a heavy air pollution episode in Shanghai, Atmos. Chem. Phys., 16, 5399-
533 5411, doi: 10.5194/acp-16-5399-2016, 2016.

534 Guo, S., Hu, M., Lin, Y., Gomez-Hernandez, M., Zamora, M. L., Peng, J., Collins, D. R., and Zhang, R.: OH-
535 Initiated Oxidation of m-Xylene on Black Carbon Aging, Environ. Sci. Technol., doi:
536 10.1021/acs.est.6b01272, 2016.

537 Hansen, J. and Nazarenko, L.: Soot climate forcing via snow and ice albedos, P Natl Acad Sci USA, 101, 423-
538 428, doi: DOI 10.1073/pnas.2237157100, 2004.

539 Herich, H., Hueglin, C., and Buchmann, B.: A 2.5 year's source apportionment study of black carbon from
540 wood burning and fossil fuel combustion at urban and rural sites in Switzerland, Atmos. Meas. Tech., 4, 1409-
541 1420, doi: DOI 10.5194/amt-4-1409-2011, 2011.

542 Hoffer, A., Gelencser, A., Guyon, P., Kiss, G., Schmid, O., Frank, G. P., Artaxo, P., and Andreae, M. O.:
543 Optical properties of humic-like substances (HULIS) in biomass-burning aerosols, Atmos. Chem. Phys., 6,
544 3563-3570, 2006.

545 Huang, X. F., Gao, R. S., Schwarz, J. P., He, L. Y., Fahey, D. W., Watts, L. A., McComiskey, A., Cooper, O.
546 R., Sun, T. L., Zeng, L. W., Hu, M., and Zhang, Y. H.: Black carbon measurements in the Pearl River Delta
547 region of China, J. Geophys. Res., 116, D12208, doi: 10.1029/2010jd014933, 2011a.

548 Huang, X. F., He, L. Y., Hu, M., Canagaratna, M. R., Kroll, J. H., Ng, N. L., Zhang, Y. H., Lin, Y., Xue, L.,
549 Sun, T. L., Liu, X. G., Shao, M., Jayne, J. T., and Worsnop, D. R.: Characterization of submicron aerosols at

Atmospheric
Chemistry
and Physics
Discussions

550 a rural site in Pearl River Delta of China using an Aerodyne High-Resolution Aerosol Mass Spectrometer,
551 Atmos. Chem. Phys., 11, 1865-1877, doi: 10.5194/acp-11-1865-2011, 2011b.
552 IPCC: Climate change 2013 : the physical science basis : Working Group I contribution to the Fifth
553 Assessment Report of the Intergovernmental Panel on Climate Change, xi, 1535 pages. pp., 2013.
554 Jason Blake, C.: Quantifying the occurrence and magnitude of the Southeast Asian fire climatology,
555 Environmental Research Letters, 9, 114018, 2014.
556 Jung, J., Lee, H., Kim, Y. J., Liu, X., Zhang, Y., Gu, J., and Fan, S.: Aerosol chemistry and the effect of
557 aerosol water content on visibility impairment and radiative forcing in Guangzhou during the 2006 Pearl River
558 Delta campaign, Journal of Environmental Management, 90, 3231-3244, doi:
559 http://dx.doi.org/10.1016/j.jenvman.2009.04.021, 2009.
560 Khalizov, A. F., Xue, H. X., Wang, L., Zheng, J., and Zhang, R. Y.: Enhanced Light Absorption and Scattering
561 by Carbon Soot Aerosol Internally Mixed with Sulfuric Acid, J Phys Chem A, 113, 1066-1074, 2009.
562 Kirchstetter, T. W., Novakov, T., and Hobbs, P. V.: Evidence that the spectral dependence of light absorption
563 by aerosols is affected by organic carbon, J. Geophys. Res., 109, D21208, doi: 10.1029/2004jd004999, 2004.
564 Knox, A., Evans, G. J., Brook, J. R., Yao, X., Jeong, C. H., Godri, K. J., Sabaliauskas, K., and Slowik, J. G.:
565 Mass Absorption Cross-Section of Ambient Black Carbon Aerosol in Relation to Chemical Age, Aerosol. Sci.
566 Technol., 43, 522-532, doi: Doi 10.1080/02786820902777207, 2009.
567 Koch, D. and Del Genio, A.: Black carbon semi-direct effects on cloud cover: review and synthesis, Atmos.
568 Chem. Phys., 10, 7685-7696, 2010.
569 Laborde, M., Mertes, P., Zieger, P., Dommen, J., Baltensperger, U., and Gysel, M.: Sensitivity of the Single
570 Particle Soot Photometer to different black carbon types, Atmos. Meas. Tech., 5, 1031-1043, 2012.
571 Lack, D. A. and Cappa, C. D.: Impact of brown and clear carbon on light absorption enhancement, single
572 scatter albedo and absorption wavelength dependence of black carbon, Atmos. Chem. Phys., 10, 4207-4220,
573 doi: DOI 10.5194/acp-10-4207-2010, 2010.
574 Lack, D. A., Langridge, J. M., Bahreini, R., Cappa, C. D., Middlebrook, A. M., and Schwarz, J. P.: Brown
575 carbon and internal mixing in biomass burning particles, P Natl Acad Sci USA, 109, 14802-14807, doi:
576 10.1073/pnas.1206575109, 2012a.
577 Lack, D. A., Richardson, M. S., Law, D., Langridge, J. M., Cappa, C. D., McLaughlin, R. J., and Murphy, D.
578 M.: Aircraft instrument for comprehensive characterization of aerosol optical properties, Part 2: black and
579 brown carbon absorption and absorption enhancement measured with photo acoustic spectroscopy, Aerosol.
580 Sci. Technol., 46, 555-568, 2012b.
581 Lack, D. A. and Langridge, J. M.: On the attribution of black and brown carbon light absorption using the
582 Ångström exponent, Atmos. Chem. Phys., 13, 10535-10543, doi: 10.5194/acp-13-10535-2013, 2013.
583 Lan, Z.-J., Huang, X.-F., Yu, K.-Y., Sun, T.-L., Zeng, L.-W., and Hu, M.: Light absorption of black carbon
584 aerosol and its enhancement by mixing state in an urban atmosphere in South China, Atmos. Environ., 69,
585 118-123, doi: http://dx.doi.org/10.1016/j.atmosenv.2012.12.009, 2013.
586 Lewis, K. A., Arnott, W. P., Moosmuller, H., Chakrabarty, R. K., Carrico, C. M., Kreidenweis, S. M., Day,
587 D. E., Malm, W. C., Laskin, A., Jimenez, J. L., Ulbrich, I. M., Huffman, J. A., Onasch, T. B., Trimborn, A.,
588 Liu, L., and Mishchenko, M. I.: Reduction in biomass burning aerosol light absorption upon humidification:
589 roles of inorganically-induced hygroscopicity, particle collapse, and photoacoustic heat and mass transfer,
590 Atmos. Chem. Phys., 9, 8949-8966, 2009.
591 Liu, D., Allan, J., Whitehead, J., Young, D., Flynn, M., Coe, H., McFiggans, G., Fleming, Z. L., and Bandy,
592 B.: Ambient black carbon particle hygroscopic properties controlled by mixing state and composition, Atmos.
593 Chem. Phys., 13, 2015-2029, doi: 10.5194/acp-13-2015-2013, 2013.

594   Liu, D., Whitehead, J., Alfarra, M. R., Reyes-Villegas, E., Spracklen, D. V., Reddington, C. L., Kong, S.,
595   Williams, P. I., Ting, Y.-C., Haslett, S., Taylor, J. W., Flynn, M. J., Morgan, W. T., McFiggans, G., Coe, H.,
596   and Allan, J. D.: Black-carbon absorption enhancement in the atmosphere determined by particle mixing state,
597   Nature Geosci, 10, 184-188, doi: 10.1038/ngeo2901

598   http://www.nature.com/ngeo/journal/v10/n3/abs/ngeo2901.html#supplementary-information, 2017.
599   Liu, S., Aiken, A. C., Gorkowski, K., Dubey, M. K., Cappa, C. D., Williams, L. R., Herndon, S. C., Massoli,
600   P., Fortner, E. C., Chhabra, P. S., Brooks, W. A., Onasch, T. B., Jayne, J. T., Worsnop, D. R., China, S.,
601   Sharma, N., Mazzoleni, C., Xu, L., Ng, N. L., Liu, D., Allan, J. D., Lee, J. D., Fleming, Z. L., Mohr, C., Zotter,
602   P., Szidat, S., and Prevot, A. S. H.: Enhanced light absorption by mixed source black and brown carbon
603   particles in UK winter, Nat Commun, 6, doi: 10.1038/ncomms9435, 2015.
604   Ma, N., Zhao, C. S., Muller, T., Cheng, Y. F., Liu, P. F., Deng, Z. Z., Xu, W. Y., Ran, L., Nekat, B., van
605   Pinxteren, D., Gnauk, T., Mueller, K., Herrmann, H., Yan, P., Zhou, X. J., and Wiedensohler, A.: A new
606   method to determine the mixing state of light absorbing carbonaceous using the measured aerosol optical
607   properties and number size distributions, Atmos. Chem. Phys., 12, 2381-2397, doi: DOI 10.5194/acp-12-
608   2381-2012, 2012.
609   Matsui, H., Koike, M., Kondo, Y., Moteki, N., Fast, J. D., and Zaveri, R. A.: Development and validation of
610   a black carbon mixing state resolved three-dimensional model: Aging processes and radiative impact, J.
611   Geophys. Res., 118, 2304-2326, doi: 10.1029/2012JD018446, 2013.
612   McMeeking, G. R., Good, N., Petters, M. D., McFiggans, G., and Coe, H.: Influences on the fraction of
613   hydrophobic and hydrophilic black carbon in the atmosphere, Atmos. Chem. Phys., 11, 5099-5112, doi:
614   10.5194/acp-11-5099-2011, 2011.
615   Moffet, R. C., O'Brien, R. E., Alpert, P. A., Kelly, S. T., Pham, D. Q., Gilles, M. K., Knopf, D. A., and Laskin,
616   A.: Morphology and mixing of black carbon particles collected in central California during the CARES field
617   study, Atmos. Chem. Phys., 16, 14515-14525, doi: 10.5194/acp-16-14515-2016, 2016.
618   Moosmuller, H., Chakrabarty, R. K., Ehlers, K. M., and Arnott, W. P.: Absorption Angstrom coefficient,
619   brown carbon, and aerosols: basic concepts, bulk matter, and spherical particles, Atmos. Chem. Phys., 11,
620   1217-1225, doi: DOI 10.5194/acp-11-1217-2011, 2011.
621   Moteki, N., Kondo, Y., and Adachi, K.: Identification by single-particle soot photometer of black carbon
622   particles attached to other particles: Laboratory experiments and ground observations in Tokyo, J. Geophys.
623   Res., 119, 2013JD020655, doi: 10.1002/2013jd020655, 2014.
624   Nakayama, T., Ikeda, Y., Sawada, Y., Setoguchi, Y., Ogawa, S., Kawana, K., Mochida, M., Ikemori, F.,
625   Matsumoto, K., and Matsumi, Y.: Properties of light-absorbing aerosols in the Nagoya urban area, Japan, in
626   August 2011 and January 2012: Contributions of brown carbon and lensing effect, J. Geophys. Res., 119,
627   2014JD021744, doi: 10.1002/2014JD021744, 2014.
628   Nordmann, S., Cheng, Y. F., Carmichael, G. R., Yu, M., Denier van der Gon, H. A. C., Zhang, Q., Saide, P.
629   E., Pöschl, U., Su, H., Birmili, W., and Wiedensohler, A.: Atmospheric black carbon and warming effects
630   influenced by the source and absorption enhancement in central Europe, Atmos. Chem. Phys., 14, 12683-
631   12699, doi: 10.5194/acp-14-12683-2014, 2014.
632   Pandolfi, M., Cusack, M., Alastuey, A., and Querol, X.: Variability of aerosol optical properties in the Western
633   Mediterranean Basin, Atmos. Chem. Phys., 11, 8189-8203, doi: DOI 10.5194/acp-11-8189-2011, 2011.
634   Peng, J., Hu, M., Guo, S., Du, Z., Zheng, J., Shang, D., Levy Zamora, M., Zeng, L., Shao, M., Wu, Y.-S.,
635   Zheng, J., Wang, Y., Glen, C. R., Collins, D. R., Molina, M. J., and Zhang, R.: Markedly enhanced absorption
636   and direct radiative forcing of black carbon under polluted urban environments, Proceedings of the National
637   Academy of Sciences, 113, 4266-4271, doi: 10.1073/pnas.1602310113, 2016.

Atmospheric
Chemistry
and Physics
Discussions

638 Pokhrel, R. P., Beamesderfer, E. R., Wagner, N. L., Langridge, J. M., Lack, D. A., Jayarathne, T., Stone, E.
639 A., Stockwell, C. E., Yokelson, R. J., and Murphy, S. M.: Relative importance of black carbon, brown carbon,
640 and absorption enhancement from clear coatings in biomass burning emissions, Atmos. Chem. Phys., 17,
641 5063-5078, doi: 10.5194/acp-17-5063-2017, 2017.

642 Ramanathan, V. and Carmichael, G.: Global and regional climate changes due to black carbon, Nat Geosci, 1,
643 221-227, doi: Doi 10.1038/Ngeo156, 2008.

644 Rose, D., Wehner, B., Ketzel, M., Engler, C., Voigtländer, J., Tuch, T., and Wiedensohler, A.: Atmospheric
645 number size distributions of soot particles and estimation of emission factors, Atmos. Chem. Phys., 6, 1021-
646 1031, doi: 10.5194/acp-6-1021-2006, 2006.

647 Saathoff, H., Naumann, K. H., Schnaiter, M., Schöck, W., Möhler, O., Schurath, U., Weingartner, E., Gysel,
648 M., and Baltensperger, U.: Coating of soot and (NH4)2SO4 particles by ozonolysis products of α-pinene, J.
649 Aerosol. Sci., 34, 1297-1321, doi: http://dx.doi.org/10.1016/S0021-8502(03)00364-1, 2003.

650 Sandradewi, J., Prévôt, A. S. H., Weingartner, E., Schmidhauser, R., Gysel, M., and Baltensperger, U.: A
651 study of wood burning and traffic aerosols in an Alpine valley using a multi-wavelength Aethalometer, Atmos.
652 Environ., 42, 101-112, doi: http://dx.doi.org/10.1016/j.atmosenv.2007.09.034, 2008.

653 Schnaiter, M., Linke, C., Mohler, O., Naumann, K. H., Saathoff, H., Wagner, R., Schurath, U., and Wehner,
654 B.: Absorption amplification of black carbon internally mixed with secondary organic aerosol, J. Geophys.
655 Res., 110, -, 2005.

656 Schwarz, J. P., Spackman, J. R., Fahey, D. W., Gao, R. S., Lohmann, U., Stier, P., Watts, L. A., Thomson, D.
657 S., Lack, D. A., Pfister, L., Mahoney, M. J., Baumgardner, D., Wilson, J. C., and Reeves, J. M.: Coatings and
658 their enhancement of black carbon light absorption in the tropical atmosphere, J. Geophys. Res., 113, -, 2008.

659 Sedlacek, A. J., Lewis, E. R., Kleinman, L., Xu, J. Z., and Zhang, Q.: Determination of and evidence for non-
660 core-shell structure of particles containing black carbon using the Single-Particle Soot Photometer (SP2),
661 Geophys.Res.Lett., 39, 2012.

662 Shen, G., Chen, Y., Wei, S., Fu, X., Zhu, Y., and Tao, S.: Mass absorption efficiency of elemental carbon for
663 source samples from residential biomass and coal combustions, Atmos. Environ., 79, 79-84, doi:
664 http://dx.doi.org/10.1016/j.atmosenv.2013.05.082, 2013.

665 Shiraiwa, M., Kondo, Y., Iwamoto, T., and Kita, K.: Amplification of Light Absorption of Black Carbon by
666 Organic Coating, Aerosol. Sci. Technol., 44, 46-54, 2010.

667 Suglia, S. F., Gryparis, A., Wright, R. O., Schwartz, J., and Wright, R. J.: Association of Black Carbon with
668 Cognition among Children in a Prospective Birth Cohort Study, American Journal of Epidemiology, 167, 280-
669 286, doi: 10.1093/aje/kwm308, 2008.

670 Tan, H., Liu, L., Fan, S., Li, F., Yin, Y., Cai, M., and Chan, P. W.: Aerosol optical properties and mixing state
671 of black carbon in the Pearl River Delta, China, Atmos. Environ., 131, 196-208, doi:
672 http://dx.doi.org/10.1016/j.atmosenv.2016.02.003, 2016.

673 Tao, W. K., Chen, J. P., Li, Z. Q., Wang, C., and Zhang, C. D.: Impact of Aerosols on Convective Clouds and
674 Precipitation, Rev Geophys, 50, Rg2001, doi: Doi 10.1029/2011rg000369, 2012.

675 ten Brink, H., Otjes, R., Jongejan, P., and Slanina, S.: An instrument for semi-continuous monitoring of the
676 size-distribution of nitrate, ammonium, sulphate and chloride in aerosol, Atmos. Environ., 41, 2768-2779, doi:
677 http://dx.doi.org/10.1016/j.atmosenv.2006.11.041, 2007.

678 Turpin, B. J. and Huntzicker, J. J.: Secondary Formation of Organic Aerosol in the Los-Angeles Basin - a
679 Descriptive Analysis of Organic and Elemental Carbon Concentrations, Atmos. Environ., 25, 207-215, 1991.

680 Ueda, S., Nakayama, T., Taketani, F., Adachi, K., Matsuki, A., Iwamoto, Y., Sadanaga, Y., and Matsumi, Y.:
681 Light absorption and morphological properties of soot-containing aerosols observed at an East Asian outflow
682 site, Noto Peninsula, Japan, Atmos. Chem. Phys., 16, 2525-2541, doi: 10.5194/acp-16-2525-2016, 2016.

Atmospheric
Chemistry
and Physics
Discussions

683   Wang, Q., Huang, R., Zhao, Z., Cao, J., Ni, H., Tie, X., Zhu, C., Shen, Z., Wang, M., and Dai, W.: Effects of
684   photochemical oxidation on the mixing state and light absorption of black carbon in the urban atmosphere of
685   China, Environmental Research Letters, 12, 044012, 2017.

686   Wang, Q. Y., Huang, R. J., Cao, J. J., Han, Y. M., Wang, G. H., Li, G. H., Wang, Y. C., Dai, W. T., Zhang,
687   R. J., and Zhou, Y. Q.: Mixing State of Black Carbon Aerosol in a Heavily Polluted Urban Area of China:
688   Implications for Light Absorption Enhancement, Aerosol. Sci. Technol., 48, 689-697, doi:
689   10.1080/02786826.2014.917758, 2014.

690   Wang, Y. Q.: MeteoInfo: GIS software for meteorological data visualization and analysis, Meteorological
691   Applications, 21, 360-368, doi: 10.1002/met.1345, 2014.

692   Weingartner, E., Saathoff, H., Schnaiter, M., Streit, N., Bitnar, B., and Baltensperger, U.: Absorption of light
693   by soot particles: determination of the absorption coefficient by means of aethalometers, J. Aerosol. Sci., 34,
694   1445-1463, doi: Doi 10.1016/S0021-8502(03)00359-8, 2003.

695   Wild, M.: Enlightening Global Dimming and Brightening, B Am Meteorol Soc, 93, 27-37, doi: 10.1175/bams-
696   d-11-00074.1, 2011.

697   Wu, C., Ng, W. M., Huang, J., Wu, D., and Yu, J. Z.: Determination of Elemental and Organic Carbon in
698   PM2.5 in the Pearl River Delta Region: Inter-Instrument (Sunset vs. DRI Model 2001 Thermal/Optical Carbon
699   Analyzer) and Inter-Protocol Comparisons (IMPROVE vs. ACE-Asia Protocol), Aerosol. Sci. Technol., 46,
700   610-621, doi: 10.1080/02786826.2011.649313, 2012.

701   Wu, C., Huang, X. H. H., Ng, W. M., Griffith, S. M., and Yu, J. Z.: Inter-comparison of NIOSH and
702   IMPROVE protocols for OC and EC determination: implications for inter-protocol data conversion, Atmos.
703   Meas. Tech., 9, 4547-4560, doi: 10.5194/amt-9-4547-2016, 2016a.

704   Wu, C. and Yu, J. Z.: Determination of primary combustion source organic carbon-to-elemental carbon
705   (OC/EC) ratio using ambient OC and EC measurements: secondary OC-EC correlation minimization method,
706   Atmos. Chem. Phys., 16, 5453-5465, doi: 10.5194/acp-16-5453-2016, 2016.

707   Wu, Cheng: Aethalometer data processor, , doi:10.5281/zenodo.832404, 2017a.

708   Wu, Cheng: Minimum R Square Method (MRS), , doi:10.5281/zenodo.832396, 2017b.

709   Wu, Cheng: Histbox, , doi:10.5281/zenodo.832411, 2017c.

710   Wu, Cheng: Scatter Plot, , doi:10.5281/zenodo.832417, 2017d.

711   Wu, Cheng: Mie Scattering, , doi:10.5281/zenodo.832400, 2017e.

712   Wu, D., Mao, J. T., Deng, X. J., Tie, X. X., Zhang, Y. H., Zeng, L. M., Li, F., Tan, H. B., Bi, X. Y., Huang,
713   X. Y., Chen, J., and Deng, T.: Black carbon aerosols and their radiative properties in the Pearl River Delta
714   region, Sci China Ser D, 52, 1152-1163, doi: 10.1007/s11430-009-0115-y, 2009.

715   Wu, D., Wu, C., Liao, B., Chen, H., Wu, M., Li, F., Tan, H., Deng, T., Li, H., Jiang, D., and Yu, J. Z.: Black
716   carbon over the South China Sea and in various continental locations in South China, Atmos. Chem. Phys.,
717   13, 12257-12270, doi: 10.5194/acp-13-12257-2013, 2013.

718   Wu, Y., Zhang, R., Tian, P., Tao, J., Hsu, S. C., Yan, P., Wang, Q., Cao, J., Zhang, X., and Xia, X.: Effect of
719   ambient humidity on the light absorption amplification of black carbon in Beijing during January 2013, Atmos.
720   Environ., 124, Part B, 217-223, doi: http://dx.doi.org/10.1016/j.atmosenv.2015.04.041, 2016b.

721   Yang, M., Howell, S. G., Zhuang, J., and Huebert, B. J.: Attribution of aerosol light absorption to black carbon,
722   brown carbon, and dust in China - interpretations of atmospheric measurements during EAST-AIRE, Atmos.
723   Chem. Phys., 9, 2035-2050, 2009.

724   Yu, H., Wu, C., Wu, D., and Yu, J. Z.: Size distributions of elemental carbon and its contribution to light
725   extinction in urban and rural locations in the pearl river delta region, China, Atmos. Chem. Phys., 10, 5107-
726   5119, doi: 10.5194/acp-10-5107-2010, 2010.

Atmospheric
Chemistry
and Physics
Discussions

Open Access

EGU

727 Zhang, G., Bi, X., Qiu, N., Han, B., Lin, Q., Peng, L., Chen, D., Wang, X., Peng, P., Sheng, G., and Zhou, Z.:
728 The real part of the refractive indices and effective densities for chemically segregated ambient aerosols in
729 Guangzhou measured by a single-particle aerosol mass spectrometer, Atmos. Chem. Phys., 16, 2631-2640,
730 doi: 10.5194/acp-16-2631-2016, 2016a.
731 Zhang, R. Y., Khalizov, A. F., Pagels, J., Zhang, D., Xue, H. X., and McMurry, P. H.: Variability in
732 morphology, hygroscopicity, and optical properties of soot aerosols during atmospheric processing, P Natl
733 Acad Sci USA, 105, 10291-10296, 2008.
734 Zhang, Y., Zhang, Q., Cheng, Y., Su, H., Kecorius, S., Wang, Z., Wu, Z., Hu, M., Zhu, T., Wiedensohler, A.,
735 and He, K.: Measuring the morphology and density of internally mixed black carbon with SP2 and VTDMA:
736 new insight into the absorption enhancement of black carbon in the atmosphere, Atmos. Meas. Tech., 9, 1833-
737 1843, doi: 10.5194/amt-9-1833-2016, 2016b.
738
739

Atmospheric
Chemistry
and Physics
Discussions

740   Table 1. Abbreviations.

741

Abbreviation	Definition
$AAE_{470\text{-}660}$	Absorption Angstrom Exponent between 470 and 660 nm
BB	Biomass burning
BrC	Brown Carbon
D_{core}, D_{shell}	Particle diameter of core/shell
E_{abs550}	Light absorption enhancement factor at 550 nm
$\sigma_{abs}550$	Light absorption coefficient at 550 nm
$\sigma_{abs,t}$	Total light absorption coefficient of a coated particle
$\sigma_{abs,p}$	Primary light absorption coefficient attributed to the soot core alone of a coated particle
$\sigma_{abs,c}$	Extra light absorption coefficient due to the lensing effect of coating on the soot core
LII	Laser induced incandescence technique for soot measurement
LWC	Liquid water content
MAE_{550}	Mass absorption efficiency at 550 nm, also known as mass absorption cross-section (MAC)
$MAE_{p,550}$	Primary MAE of freshly emitted soot particles at 550 nm
MAAP	Multi Angle Absorption Photometer
MOUDI	Micro Orifice Uniform Deposit Impactor
MRS	Minimum R squared method
PAS	Photo acoustic spectrometer
PRD	Pearl River Delta region, China
SP2	Single particle soot photometer
SSA	Single scattering albedo
TD	Thermal denuder
TOA	Thermal optical analysis
TSV	Total spatial variance in backward trajectories cluster analysis

742

Atmospheric
Chemistry
and Physics
Discussions

Open Access

743   Table 2. Comparison of MRS application on $(OC/EC)_p$ (for SOC estimation) and MAE_p (for E_{abs} estimation).

744

	MRS in EC tracer method for SOC estimation (Wu and Yu, 2016)	MRS in EC tracer method for E_{abs} estimation (this study)
Key parameter of fresh EC particles to be determined	$(\frac{OC}{EC})_p = \frac{POC}{EC}$	$MAE_p = \frac{O\sigma_{abs,p}}{EC}$
Input quantities for MRS from measurements	OC, EC (tracer)	$\sigma_{abs,t}$, EC (tracer)
Variable to be decoupled by the tracer	OC=POC+SOC $=(\frac{OC}{EC})_p \times EC + SOC$	$\sigma_{abs,t} = \sigma_{abs,p} + \sigma_{abs,c}$ $=(\frac{O\sigma_{abs,t}C}{EC})_p \times EC + \sigma_{abs,c}$
Ambient measurement at its closest to fresh emissions	Minimum R^2 (SOC, EC) $SOC = OC - (\frac{OC}{EC})_p \times EC$	Minimum R^2 ($\sigma_{abs,c}$, EC) $\sigma_{abs,c} = \sigma_{abs,t} - MAE_p \times EC$
Graph		

745

746   Table 3. Comparison of E_{abs} between various studies.

747

Location	Type	Sampling Duration	λ (nm)	Instrument	E_{abs}	Method	Reference
Guangzhou, China	Suburban	2012.2-2013.1	550	AE	1.52±0.51	MAE	This study
Xi'an, China	Urban	2012.12-2013.1	870	PAS	1.8	MAE	(Wang et al., 2014)
Shenzhen, China	Urban	2011.8-9	532	PAS	1.3	MAE	(Lan et al., 2013)
Jinan, China	Urban	2014.2	678	OCEC	2.07 ± 0.72	AFD	(Chen et al., 2017)
Nanjing, China	Suburban	2012.11	532	PAS	1.6	MAE	(Cui et al., 2016a)
Boulder, USA	Forest fire	2010.9	532	PAS	1.38	TD 200℃	(Lack et al., 2012a)
London, UK	Rural	2012.2	781	PAS	1.4	TD 250℃	(Liu et al., 2015)
California, USA	Rural	2010.6	532	PAS	1.06	TD 250℃	(Cappa et al., 2012)
Noto Peninsula, Japan	Rural	2013.4-5	781	PAS	1.22	TD 300℃	(Ueda et al., 2016)
Yuncheng, China	Rural	2014.6-7	678	OCEC	2.25 ± 0.55	AFD	(Cui et al., 2016b)
San Jose, Costa Rica	Rural	2006 winter	1064	SP2	1.3	Mie+SP2	(Schwarz et al., 2008)

748   AE: Aethalometer ; PAS photo acoustic spectrometer; SP2: Single particle soot photometer; TD: Thermal denuder

749

Atmospheric
Chemistry
and Physics
Discussions

750
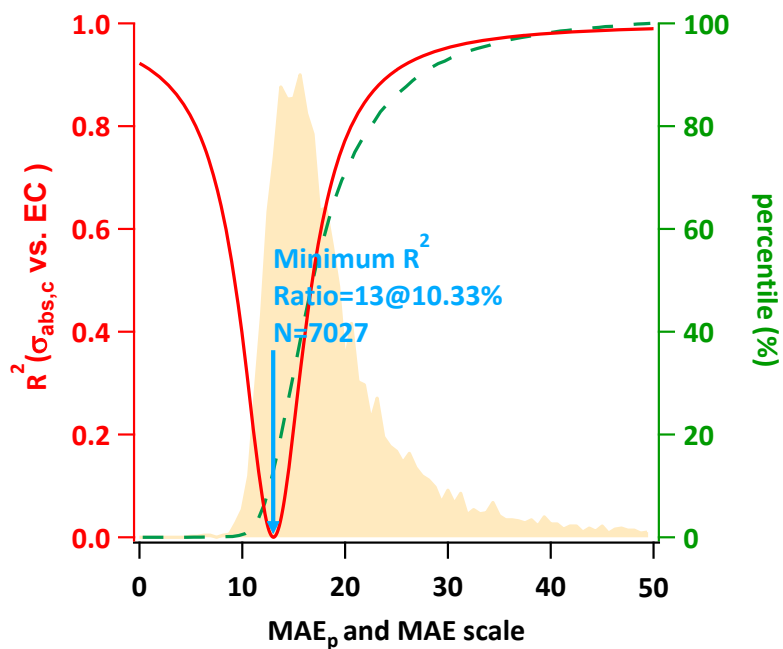
Figure 1. Minimum R squared (MRS) plot for calculating MAE_p. The red curve is the correlation result between $\sigma_{abs,c}$ ($\sigma_{abs,t}$ − $EC * MAE_p$) and EC mass. The shaded area in light tan represents the frequency distribution of observed MAE. The dashed green line is the cumulative distribution of observed MAE.

Atmospheric
Chemistry
and Physics
Discussions

Open Access

754
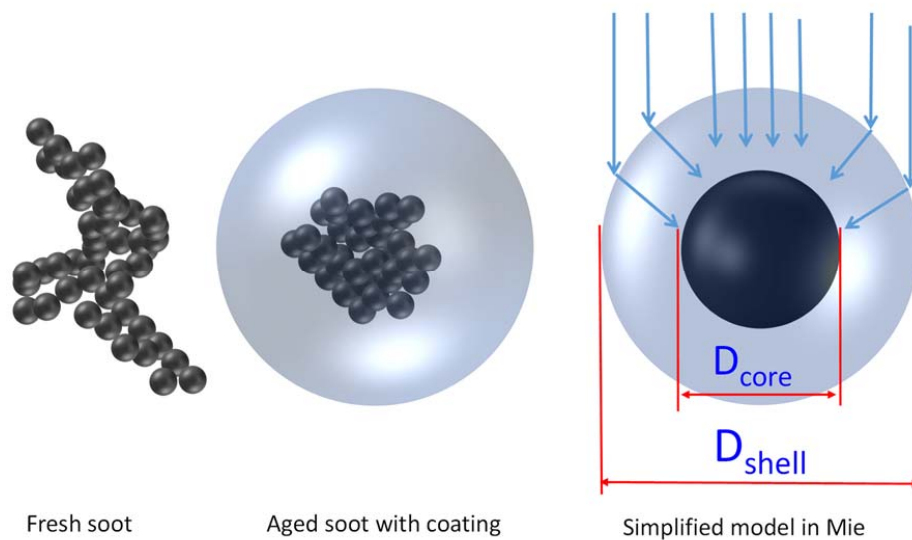
Figure 2. Schematic of the aging effect on light absorption. More light is absorbed by the soot particle core due to the lensing effect
of the coating materials.

757

Atmospheric
Chemistry
and Physics
Discussions

Open Access

758
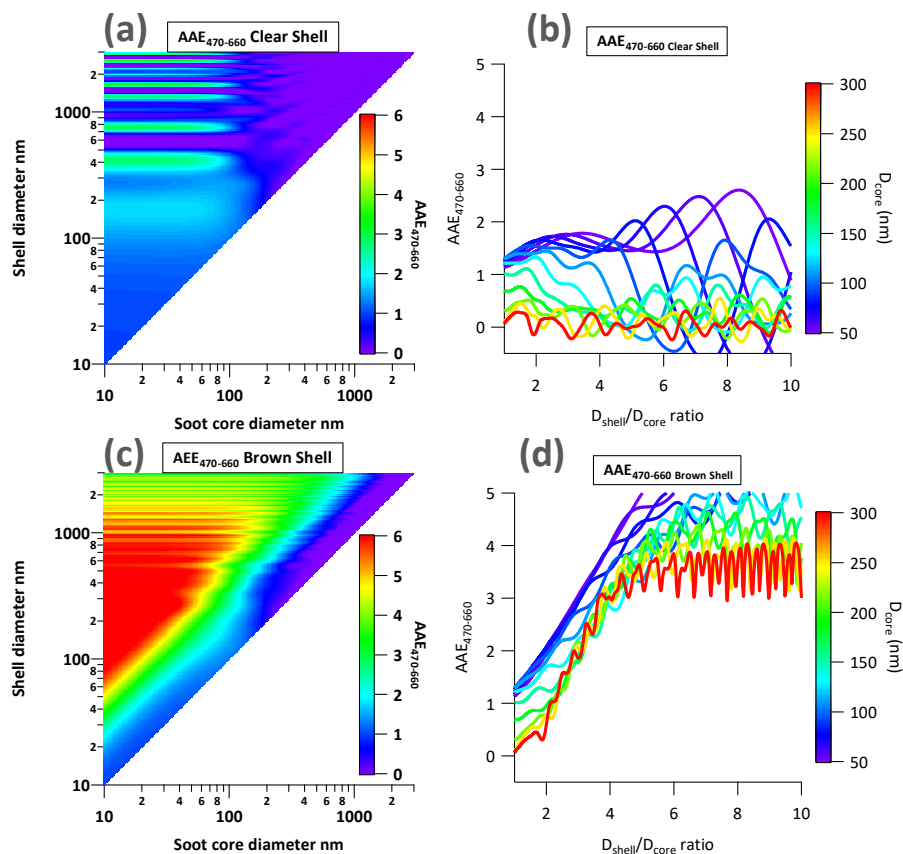
Figure 3. Mie simulated size dependency of soot particles $AAE_{470-660}$. (a) Combination of different shell (y axis) and core diameters (x axis). The color coding represents the $AAE_{470-660}$ of a particle with specific core and shell size; (b) Cross-sections views of (a). The color coding represents different D_{core} in the range of 50 ∼ 300 nm. (c) Combination of different shell (y axis) and core diameters (x axis). The color coding represents the $AAE_{470-660}$ of a particle with specific core and shell size; (d) Cross-sectional views of (c) The color coding represents different D_{core} in the range of 50 – 300 nm.

759
760
761
762
763
764
765
766

Atmospheric
Chemistry
and Physics
Discussions

767
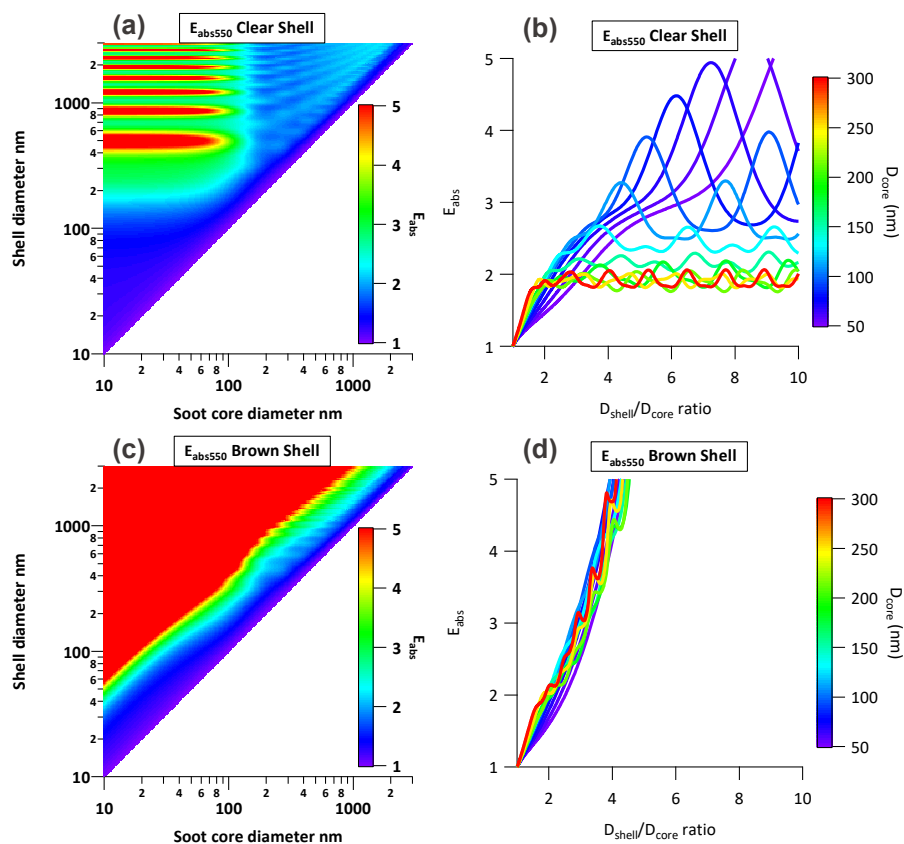
Figure 4. Mie simulated size dependency of soot particles E_{abs} at wavelength 550 nm. (a)Combination of different shell (y axis) and
core diameters (x axis). The color coding represents the E_{abs} of a particle with specific core and shell size; (b) Cross-sections views
of (a). The color coding represents different D_{core} in the range of 50 – 300 nm. (c)Combination of different shell (y axis) and core
diameters (x axis). The color coding represents the E_{abs} of a particle with specific core and shell size; (d) Cross-sectional views of
(c). The color coding represents different D_{core} in the range of 50 – 300 nm.

773

774

775
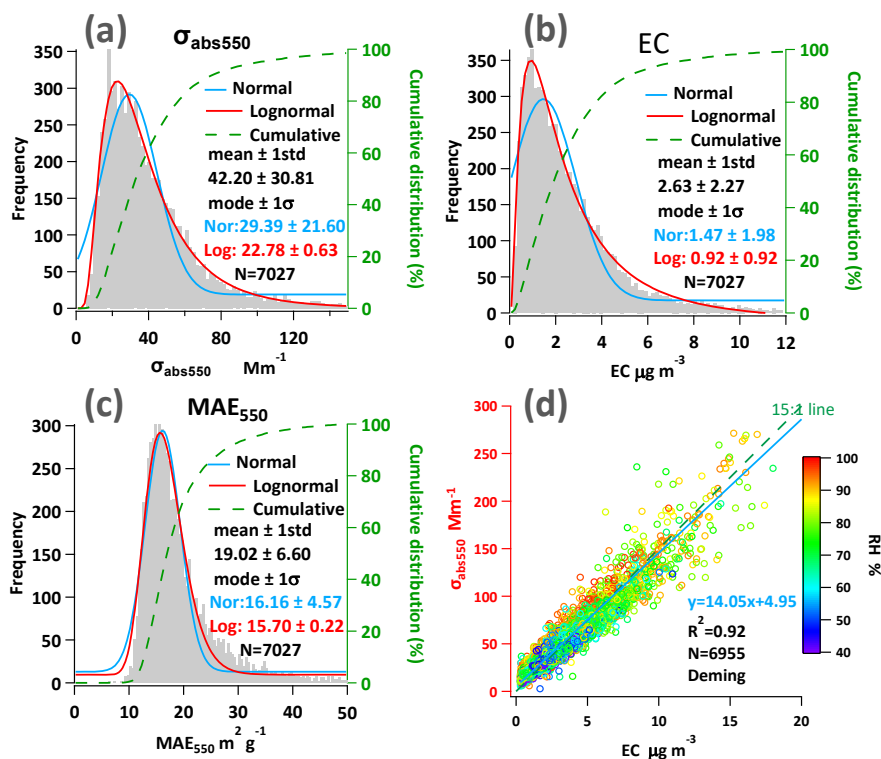
Figure 5. Measured annual statistics of σ_{abs550}, EC and MAE$_{550}$. (a) Annual frequency distribution of light absorption at 550 nm. The blue curve represents the fitting line for Gaussian distribution while the red curve represents the fitting line for a log-normal distribution. (b) Annual frequency distribution of EC mass concentration (c) Frequency distribution of Mass absorption efficiency (MAE) at 550 nm. (d) Scatter plot of light absorption (550 nm) and EC mass. The slope represents MAE. The blue regression line is by Deming regression. The color coding represents RH.

Atmospheric
Chemistry
and Physics
Discussions
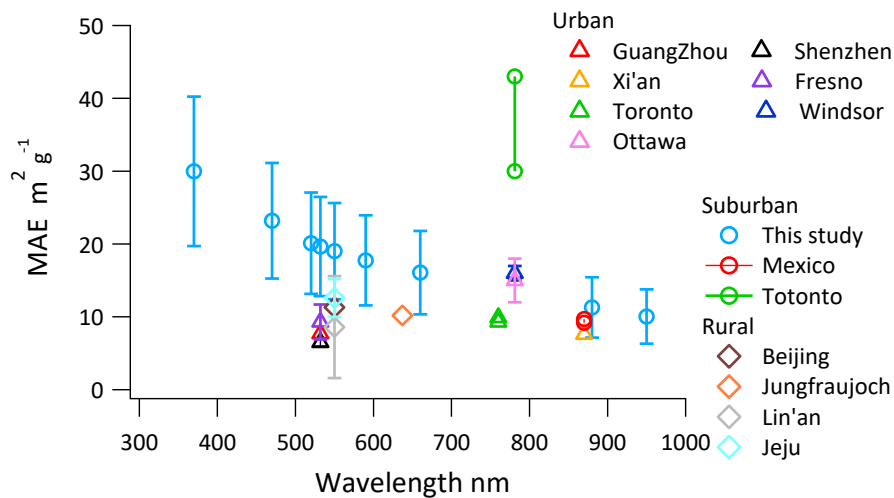
783

784   Figure 6. Comparison of spectral MAE measurements from this study with previous studies. Triangle, circle and rhombus represent

785   urban, suburban and rural respectively. The whiskers represent one standard deviation.

786
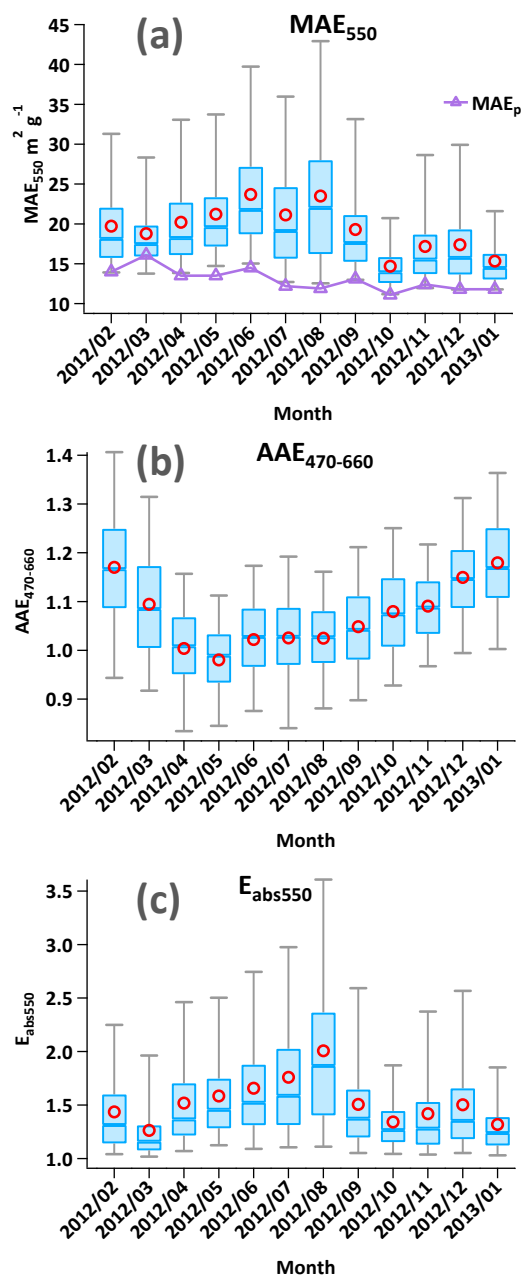
Figure 7. Measured monthly variations of (a) MAE_{550}, the purple line represents MAE_p estimated by MRS (b) $AAE_{470-660}$ and (c) E_{abs550}. Red circles represent the monthly average. The line inside the box indicates the monthly median. Upper and lower boundaries of the box represent the 75th and the 25th percentiles; the whiskers above and below each box represent the 95th and 5th percentiles.
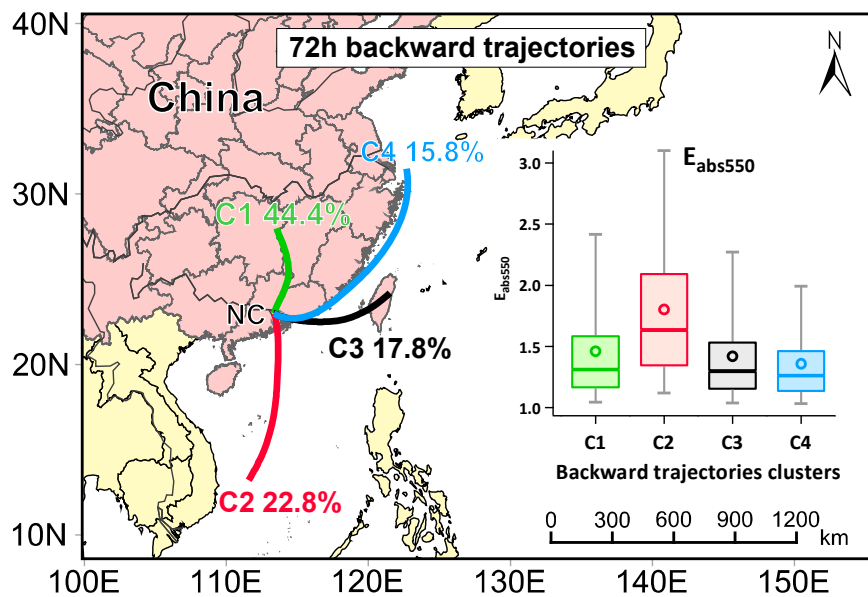
Figure 8. Average backward trajectories arriving at 100 m at NC site for four clusters (2012 Feb - 2013 Jan). E_{abs550} by different clusters are shown in the box plot.

793
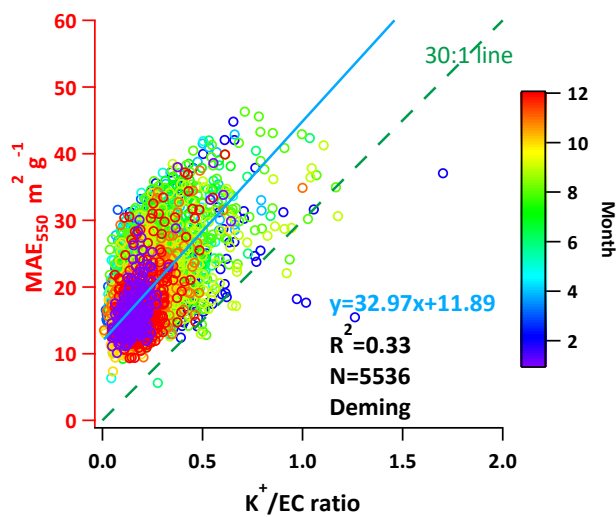
Figure 9. MAE_{550} dependency on biomass burning indicator K^+/EC ratio. The color coding represents months. The intercept

795   represents MAE without biomass burning effect.

Atmospheric
Chemistry
and Physics
Discussions

796
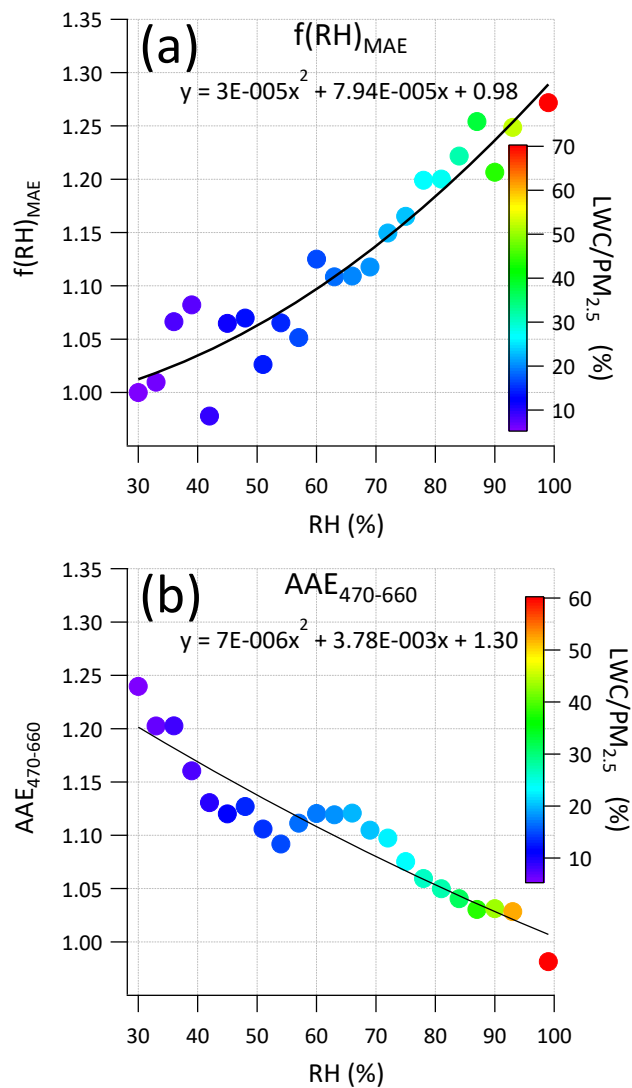
Figure 10. Optical properties dependency on RH determined from one year's sampling data at NC site. (a) Hygroscopic growth
factor (f(RH)) of EC MAE (b) $AAE_{470-660}$ as a function of RH.